Kinematic dependence of azimuthal anisotropies in p+Au, d+Au, and He3+Au at √sNN=200GeV

(PHENIX Collaboration) Acharya, U. A.; Adare, A.; Aidala, C.; Ajitanand, N. N.; Akiba, Y.; Alfred, M.; Andrieux, V.; Aoki, K.; Apadula, N.; Asano, H.; ...

Source / Izvornik: **Physical Review C, 2022, 105**

Journal article, Published version
Rad u časopisu, Objavljena verzija rada (izdavačev PDF)

https://doi.org/10.1103/PhysRevC.105.024901

Permanent link / Trajna poveznica: https://urn.nsk.hr/urn:nbn:hr:217:439250

Kinematic dependence of azimuthal anisotropies in $p + \mathrm{Au}$, $d + \mathrm{Au}$, and $^3\mathrm{He} + \mathrm{Au}$ at $\sqrt{s_{NN}} = 200$ GeV

U. A. Acharya,[21] A. Adare,[12] C. Aidala,[42] N. N. Ajitanand,[60,*] Y. Akiba,[55,56,†] M. Alfred,[23] V. Andrieux,[42] K. Aoki,[32,55] N. Apadula,[28,61] H. Asano,[35,55] C. Ayuso,[42] B. Azmoun,[7] V. Babintsev,[24] M. Bai,[6] N. S. Bandara,[41] B. Bannier,[61] K. N. Barish,[8] S. Bathe,[5,56] A. Bazilevsky,[7] M. Beaumier,[8] S. Beckman,[12] R. Belmont,[12,42,48] A. Berdnikov,[58] Y. Berdnikov,[58] L. Bichon,[66] B. Blankenship,[66] D. S. Blau,[34,45] M. Boer,[37] J. S. Bok,[47] V. Borisov,[58] K. Boyle,[56] M. L. Brooks,[37] J. Bryslawskyj,[5,8] V. Bumazhnov,[24] C. Butler,[21] S. Campbell,[13,28] V. Canoa Roman,[61] R. Cervantes,[61] C.-H. Chen,[56] M. Chiu,[7] C. Y. Chi,[13] I. J. Choi,[25] J. B. Choi,[30,*] T. Chujo,[65] Z. Citron,[67] M. Connors,[21,56] R. Corliss,[61] N. Cronin,[43,61] T. Csörgő,[17,68] M. Csanád,[16] L. D. Liu,[52] T. W. Danley,[49] A. Datta,[46] M. S. Daugherity,[1] G. David,[7,61] K. DeBlasio,[46] K. Dehmelt,[61] A. Denisov,[24] A. Deshpande,[56,61] E. J. Desmond,[7] A. Dion,[61] P. B. Diss,[40] D. Dixit,[61] J. H. Do,[69] A. Drees,[61] K. A. Drees,[6] M. Dumancic,[67] J. M. Durham,[37] A. Durum,[24] T. Elder,[21] H. En'yo,[55] A. Enokizono,[55,57] R. Esha,[61] S. Esumi,[65] B. Fadem,[43] W. Fan,[61] N. Feege,[61] D. E. Fields,[46] M. Finger, Jr.,[9] M. Finger,[9] D. Fitzgerald,[42] S. L. Fokin,[34] J. E. Frantz,[49] A. Franz,[7] A. D. Frawley,[20] Y. Fukuda,[65] P. Gallus,[14] C. Gal,[61] P. Garg,[3,61] H. Ge,[61] M. Giles,[61] F. Giordano,[25] A. Glenn,[36] Y. Goto,[55,56] N. Grau,[2] S. V. Greene,[66] M. Grosse Perdekamp,[25] T. Gunji,[11] H. Guragain,[21] T. Hachiya,[44,55,56] J. S. Haggerty,[7] K. I. Hahn,[18] H. Hamagaki,[11] H. F. Hamilton,[1] J. Hanks,[61] S. Y. Han,[18,33] M. Harvey,[63] S. Hasegawa,[29] T. O. S. Haseler,[21] K. Hashimoto,[55,57] T. K. Hemmick,[61] X. He,[21] J. C. Hill,[28] K. Hill,[12] A. Hodges,[21] R. S. Hollis,[8] K. Homma,[22] B. Hong,[33] T. Hoshino,[22] N. Hotvedt,[28] J. Huang,[7] K. Imai,[29] J. Imrek,[15] M. Inaba,[65] A. Iordanova,[8] D. Isenhower,[1] Y. Ito,[44] D. Ivanishchev,[53] B. V. Jacak,[61] M. Jezghani,[21] X. Jiang,[37] Z. Ji,[61] B. M. Johnson,[7,21] V. Jorjadze,[61] D. Jouan,[51] D. S. Jumper,[25] S. Kanda,[11] J. H. Kang,[69] D. Kapukchyan,[8] S. Karthas,[61] D. Kawall,[41] A. V. Kazantsev,[34] J. A. Key,[46] V. Khachatryan,[61] A. Khanzadeev,[53] A. Khatiwada,[37] B. Kimelman,[43] C. Kim,[8,33] D. J. Kim,[31] E.-J. Kim,[30] G. W. Kim,[18] M. Kim,[59] M. H. Kim,[33] T. Kim,[18] D. Kincses,[16] A. Kingan,[61] E. Kistenev,[7] R. Kitamura,[11] J. Klatsky,[20] D. Kleinjan,[8] P. Kline,[61] T. Koblesky,[12] B. Komkov,[53] D. Kotov,[53,58] L. Kovacs,[16] S. Kudo,[65] B. Kurgyis,[16] K. Kurita,[57] M. Kurosawa,[55,56] Y. Kwon,[69] J. G. Lajoie,[28] E. O. Lallow,[43] D. Larionova,[58] A. Lebedev,[28] S. Lee,[69] S. H. Lee,[28,42,61] M. J. Leitch,[37] Y. H. Leung,[61] N. A. Lewis,[42] S. H. Lim,[37,54,69] M. X. Liu,[37] X. Li,[10] X. Li,[37] V.-R. Loggins,[25] S. Lökös,[16] D. A. Loomis,[42] K. Lovasz,[15] D. Lynch,[7] T. Majoros,[15] Y. I. Makdisi,[6] M. Makek,[70] M. Malaev,[53] A. Manion,[61] V. I. Manko,[34] E. Mannel,[7] H. Masuda,[57] M. McCumber,[37] P. L. McGaughey,[37] D. McGlinchey,[12,37] C. McKinney,[25] A. Meles,[47] M. Mendoza,[8] A. C. Mignerey,[40] D. E. Mihalik,[61] A. Milov,[67] D. K. Mishra,[4] J. T. Mitchell,[7] M. Mitrankova,[58] Iu. Mitrankov,[58] G. Mitsuka,[32,56] S. Miyasaka,[55,64] S. Mizuno,[55,65] A. K. Mohanty,[4] M. M. Mondal,[61] P. Montuenga,[25] T. Moon,[33,69] D. P. Morrison,[7] S. I. Morrow,[66] T. V. Moukhanova,[34] B. Mulilo,[33,55] T. Murakami,[35,55] J. Murata,[55,57] A. Mwai,[60] K. Nagai,[64] K. Nagashima,[22] T. Nagashima,[57] J. L. Nagle,[12] M. I. Nagy,[16] I. Nakagawa,[55,56] H. Nakagomi,[55,65] K. Nakano,[55,64] C. Nattrass,[62] S. Nelson,[19] P. K. Netrakanti,[4] T. Niida,[65] S. Nishimura,[11] R. Nouicer,[7,56] T. Novák,[17,68] N. Novitzky,[31,61,65] R. Novotny,[14] G. Nukazuka,[55,56] A. S. Nyanin,[34] E. O'Brien,[7] C. A. Ogilvie,[28] J. D. Orjuela Koop,[12] J. D. Osborn,[42,50] A. Oskarsson,[38] G. J. Ottino,[46] K. Ozawa,[32,65] R. Pak,[7] V. Pantuev,[26] V. Papavassiliou,[47] J. S. Park,[59] S. Park,[55,59,61] M. Patel,[28] S. F. Pate,[47] J.-C. Peng,[25] W. Peng,[66] D. V. Perepelitsa,[7,12] G. D. N. Perera,[47] D. Yu. Peressounko,[34] C. E. PerezLara,[61] J. Perry,[28] R. Petti,[7,61] M. Phipps,[7,25] C. Pinkenburg,[7] R. Pinson,[1] R. P. Pisani,[7] M. Potekhin,[7] A. Pun,[49] M. L. Purschke,[7] P. V. Radzevich,[58] J. Rak,[31] N. Ramasubramanian,[61] B. J. Ramson,[42] I. Ravinovich,[67] K. F. Read,[50,62] D. Reynolds,[60] V. Riabov,[45,53] Y. Riabov,[53,58] D. Richford,[5] T. Rinn,[25,28] S. D. Rolnick,[8] M. Rosati,[28] Z. Rowan,[5] J. G. Rubin,[42] J. Runchey,[28] A. S. Safonov,[58] B. Sahlmueller,[61] N. Saito,[32] T. Sakaguchi,[7] H. Sako,[29] V. Samsonov,[45,53] M. Sarsour,[21] K. Sato,[65] S. Sato,[29] B. Schaefer,[66] B. K. Schmoll,[62] K. Sedgwick,[8] R. Seidl,[55,56] A. Sen,[28,62] R. Seto,[8] P. Sett,[4] A. Sexton,[40] D. Sharma,[61] I. Shein,[24] T.-A. Shibata,[55,64] K. Shigaki,[22] M. Shimomura,[28,44] T. Shioya,[65] P. Shukla,[4] A. Sickles,[7,25] C. L. Silva,[37] D. Silvermyr,[38,50] B. K. Singh,[3] C. P. Singh,[3] V. Singh,[3] M. Slunečka,[9] K. L. Smith,[20] M. Snowball,[37] R. A. Soltz,[36] W. E. Sondheim,[37] S. P. Sorensen,[62] I. V. Sourikova,[7] P. W. Stankus,[50] M. Stepanov,[41,*] S. P. Stoll,[7] T. Sugitate,[22] A. Sukhanov,[7] T. Sumita,[55] J. Sun,[61] Z. Sun,[15] S. Syed,[21] J. Sziklai,[68] A. Takeda,[44] A. Taketani,[55,56] K. Tanida,[29,56,59] M. J. Tannenbaum,[7] S. Tarafdar,[66,67] A. Taranenko,[45,60] G. Tarnai,[15] R. Tieulent,[21,39] A. Timilsina,[28] T. Todoroki,[55,56,65] M. Tomášek,[14] C. L. Towell,[1] R. Towell,[1] R. S. Towell,[1] I. Tserruya,[67] Y. Ueda,[22] B. Ujvari,[15] H. W. van Hecke,[37] S. Vazquez-Carson,[12] J. Velkovska,[66] M. Virius,[14] V. Vrba,[14,27] N. Vukman,[70] X. R. Wang,[47,56] Z. Wang,[5] Y. Watanabe,[55,56] Y. S. Watanabe,[11,32] F. Wei,[47] A. S. White,[42] C. P. Wong,[21,37] C. L. Woody,[7] M. Wysocki,[50]

[*] Deceased.

[†] PHENIX Spokesperson: akiba@rcf.rhic.bnl.gov

B. Xia,[49] L. Xue,[21] C. Xu,[47] Q. Xu,[66] S. Yalcin,[61] Y. L. Yamaguchi,[11,56,61] H. Yamamoto,[65] A. Yanovich,[24] P. Yin,[12] I. Yoon,[59] J. H. Yoo,[33] I. E. Yushmanov,[34] H. Yu,[47,52] W. A. Zajc,[13] A. Zelenski,[6] S. Zharko,[58] S. Zhou,[10] and L. Zou[8]
(PHENIX Collaboration)

[1]*Abilene Christian University, Abilene, Texas 79699, USA*
[2]*Department of Physics, Augustana University, Sioux Falls, South Dakota 57197, USA*
[3]*Department of Physics, Banaras Hindu University, Varanasi 221005, India*
[4]*Bhabha Atomic Research Centre, Bombay 400 085, India*
[5]*Baruch College, City University of New York, New York, New York 10010, USA*
[6]*Collider-Accelerator Department, Brookhaven National Laboratory, Upton, New York 11973-5000, USA*
[7]*Physics Department, Brookhaven National Laboratory, Upton, New York 11973-5000, USA*
[8]*University of California-Riverside, Riverside, California 92521, USA*
[9]*Charles University, Ovocný trh 5, Praha 1, 116 36 Prague, Czech Republic*
[10]*Science and Technology on Nuclear Data Laboratory, China Institute of Atomic Energy, Beijing 102413, People's Republic of China*
[11]*Center for Nuclear Study, Graduate School of Science, University of Tokyo, 7-3-1 Hongo, Bunkyo, Tokyo 113-0033, Japan*
[12]*University of Colorado, Boulder, Colorado 80309, USA*
[13]*Columbia University, New York, New York 10027 and Nevis Laboratories, Irvington, New York 10533, USA*
[14]*Czech Technical University, Zikova 4, 166 36 Prague 6, Czech Republic*
[15]*Debrecen University, Egyetem tér 1, H-4010 Debrecen, Hungary*
[16]*ELTE, Eötvös Loránd University, Pázmány P.s. 1/A, H-1117 Budapest, Hungary*
[17]*Eszterházy Károly University, Károly Róbert Campus, Mátrai út 36, H-3200 Gyöngyös, Hungary*
[18]*Ewha Womans University, Seoul 120-750, Korea*
[19]*Florida A&M University, Tallahassee, Florida 32307, USA*
[20]*Florida State University, Tallahassee, Florida 32306, USA*
[21]*Georgia State University, Atlanta, Georgia 30303, USA*
[22]*Hiroshima University, Kagamiyama, Higashi-Hiroshima 739-8526, Japan*
[23]*Department of Physics and Astronomy, Howard University, Washington, DC 20059, USA*
[24]*IHEP Protvino, State Research Center of Russian Federation, Institute for High Energy Physics, Protvino 142281, Russia*
[25]*University of Illinois at Urbana-Champaign, Urbana, Illinois 61801, USA*
[26]*Institute for Nuclear Research of the Russian Academy of Sciences, Prospekt 60-Letiya Oktyabrya 7a, Moscow 117312, Russia*
[27]*Institute of Physics, Academy of Sciences of the Czech Republic, Na Slovance 2, 182 21 Prague 8, Czech Republic*
[28]*Iowa State University, Ames, Iowa 50011, USA*
[29]*Advanced Science Research Center, Japan Atomic Energy Agency, 2-4 Shirakata Shirane, Tokai-mura, Naka-gun, Ibaraki-ken 319-1195, Japan*
[30]*Jeonbuk National University, Jeonju, 54896, Korea*
[31]*Helsinki Institute of Physics and University of Jyväskylä, P.O. Box 35, FI-40014 Jyväskylä, Finland*
[32]*KEK, High Energy Accelerator Research Organization, Tsukuba, Ibaraki 305-0801, Japan*
[33]*Korea University, Seoul 02841, Korea*
[34]*National Research Center "Kurchatov Institute", Moscow 123098, Russia*
[35]*Kyoto University, Kyoto 606-8502, Japan*
[36]*Lawrence Livermore National Laboratory, Livermore, California 94550, USA*
[37]*Los Alamos National Laboratory, Los Alamos, New Mexico 87545, USA*
[38]*Department of Physics, Lund University, Box 118, SE-221 00 Lund, Sweden*
[39]*IPNL, CNRS/IN2P3, Université Lyon 1, F-69622, Villeurbanne, France*
[40]*University of Maryland, College Park, Maryland 20742, USA*
[41]*Department of Physics, University of Massachusetts, Amherst, Massachusetts 01003-9337, USA*
[42]*Department of Physics, University of Michigan, Ann Arbor, Michigan 48109-1040, USA*
[43]*Muhlenberg College, Allentown, Pennsylvania 18104-5586, USA*
[44]*Nara Women's University, Kita-uoya Nishi-machi, Nara 630-8506, Japan*
[45]*National Research Nuclear University, MEPhI, Moscow Engineering Physics Institute, Moscow 115409, Russia*
[46]*University of New Mexico, Albuquerque, New Mexico 87131, USA*
[47]*New Mexico State University, Las Cruces, New Mexico 88003, USA*
[48]*Physics and Astronomy Department, University of North Carolina at Greensboro, Greensboro, North Carolina 27412, USA*
[49]*Department of Physics and Astronomy, Ohio University, Athens, Ohio 45701, USA*
[50]*Oak Ridge National Laboratory, Oak Ridge, Tennessee 37831, USA*
[51]*IPN-Orsay, Université Paris-Sud, CNRS/IN2P3, Université Paris-Saclay, BP 1, F-91406 Orsay, France*
[52]*Peking University, Beijing 100871, People's Republic of China*
[53]*PNPI, Petersburg Nuclear Physics Institute, Gatchina, Leningrad Region 188300, Russia*

[54]*Pusan National University, Pusan 46241, Korea*
[55]*RIKEN Nishina Center for Accelerator-Based Science, Wako, Saitama 351-0198, Japan*
[56]*RIKEN BNL Research Center, Brookhaven National Laboratory, Upton, New York 11973-5000, USA*
[57]*Physics Department, Rikkyo University, 3-34-1 Nishi-Ikebukuro, Toshima, Tokyo 171-8501, Japan*
[58]*Saint Petersburg State Polytechnic University, St. Petersburg 195251, Russia*
[59]*Department of Physics and Astronomy, Seoul National University, Seoul 151-742, Korea*
[60]*Chemistry Department, Stony Brook University, SUNY, Stony Brook, New York 11794-3400, USA*
[61]*Department of Physics and Astronomy, Stony Brook University, SUNY, Stony Brook, New York 11794-3800, USA*
[62]*University of Tennessee, Knoxville, Tennessee 37996, USA*
[63]*Texas Southern University, Houston, Texas 77004, USA*
[64]*Department of Physics, Tokyo Institute of Technology, Oh-okayama, Meguro, Tokyo 152-8551, Japan*
[65]*Tomonaga Center for the History of the Universe, University of Tsukuba, Tsukuba, Ibaraki 305, Japan*
[66]*Vanderbilt University, Nashville, Tennessee 37235, USA*
[67]*Weizmann Institute, Rehovot 76100, Israel*
[68]*Institute for Particle and Nuclear Physics, Wigner Research Centre for Physics, Hungarian Academy of Sciences (Wigner RCP, RMKI), P.O. Box 49, H-1525 Budapest 114, Budapest, Hungary*
[69]*Yonsei University, IPAP, Seoul 120-749, Korea*
[70]*Department of Physics, Faculty of Science, University of Zagreb, Bijenička c. 32 HR-10002 Zagreb, Croatia*

(Received 15 July 2021; revised 16 November 2021; accepted 5 January 2022; published 3 February 2022)

There is strong evidence for the formation of small droplets of quark-gluon plasma in $p/d/^3$He +Au collisions at the Relativistic Heavy Ion Collider (RHIC) and in $p+p$/Pb collisions at the Large Hadron Collider. In particular, the analysis of data at RHIC for different geometries obtained by varying the projectile size and shape has proved insightful. In the present analysis, we find excellent agreement with the previously published PHENIX at RHIC results on elliptical and triangular flow with an independent analysis via the two-particle correlation method, which has quite different systematic uncertainties and an independent code base. In addition, the results are extended to other detector combinations with different kinematic (pseudorapidity) coverage. These results provide additional constraints on contributions from nonflow and longitudinal decorrelations.

DOI: 10.1103/PhysRevC.105.024901

I. INTRODUCTION

The Relativistic Heavy Ion Collider (RHIC) was built and the Large Hadron Collider (LHC) heavy-ion program initiated to study the formation of nucleus-sized droplets of quark-gluon plasma (QGP) in the laboratory. This focused scientific enterprise has been remarkably successful. The now standard model of heavy-ion collisions includes the formation of QGP that expands hydrodynamically before the phase transition to hadrons with confined quarks and gluons. References [1–3] provide useful reviews. Over the past ten years, experiments have employed multiple techniques to assess whether such QGP droplets are also formed in smaller $p+A$ and even $p+p$ collisions; see Ref. [4] for a recent review.

A specific proposal was to collide proton, deuteron, and helium-3 projectiles on nuclear targets at RHIC, utilizing the unique capabilities of that facility, to discern whether "flow-like" patterns are indeed attributable to mini-QGP droplet formation [5]. In the years 2014, 2015, and 2016, RHIC provided collisions of ^{3}He +Au, $p+$ Au, and $d+$ Au at $\sqrt{s_{NN}} =$ 200 GeV, extending earlier results from 2003 and 2008 $d+$ Au runs. The PHENIX Collaboration has published a suite of results on small systems including transverse momentum (p_T) spectra of identified particles (indicating "baryon anomaly" results in small collision systems) [6], pseudorapidity dependence of particle production and anisotropy coefficients [7,8], multiparticle cumulants [9], and anisotropy coefficients at midrapidity as a function of p_T for charged hadrons [10–13] and for identified particles [14,15]. The full set of elliptic and triangular azimuthal anisotropy coefficients (v_2 and v_3, respectively) for all three collision geometries were published in Nature Physics [16].

The elliptical and triangular azimuthal anisotropy coefficients in all three collision geometries are quantitatively predicted by viscous hydrodynamic calculations published prior to the data [5,17]. After intense theoretical work [18,19] and intense scientific scrutiny [20], calculations with initial-state correlations in the color glass condensate framework are definitively ruled out as the dominant source of the observed correlations. More recent calculations indicate that prehydrodynamization evolution, either in the weak [21] or strong [22] coupling limit, may have a significant impact on the shortest lifetime systems—including the smallest systems or any size system at the lowest energies—particularly for triangular flow. Additionally, calculations within parton transport frameworks such as the AMPT (A Multi-Phase Transport) model qualitatively reproduce the flow coefficient ordering [23]. Finally, the initial geometry has contributions from both intrinsic geometry and from geometric fluctuations (originating from nucleonic and subnucleonic position-space fluctuations), and from the statistics of particle production. As an example, the initial spatial eccentricities ε_2 and ε_3 for central collisions (impact parameter $b < 2$ fm) in different

TABLE I. Summary of various initial geometry calculations quantified by the average eccentricities $\varepsilon_{2,3}$ in central (impact parameter $b < 2$ fm) $p+$Au, $d+$Au, and ^{3}He$+$Au events. The "Nucl. without NBD fluc." column refers to Monte Carlo Glauber with nucleon position fluctuations [5]. The "Nucl. with NBD fluc." column refers to Monte Carlo Glauber with nucleon position fluctuations and negative binomial distribution (NBD) fluctuations in particle production [24]. The "Quarks with NBD fluc." column refers to Monte Carlo Glauber with constituent quark position fluctuations and NBD fluctuations [24]. The last two columns use the IP-Glasma framework including gluon field fluctuations [25] in publicly available code with nucleon and constituent quark position fluctuations.

$\langle\varepsilon_{2,3}\rangle$	Collision system	Nucl. without NBD fluc.	Nucl. with NBD fluc.	Quarks with NBD fluc.	IP-G with nucl.	IP-G with quarks
$\langle\varepsilon_2\rangle$	$p+$Au	0.23	0.32	0.38	0.10	0.50
	$d+$Au	0.54	0.48	0.51	0.58	0.73
	^{3}He$+$Au	0.50	0.50	0.52	0.55	0.64
$\langle\varepsilon_3\rangle$	$p+$Au	0.16	0.24	0.30	0.09	0.32
	$d+$Au	0.18	0.28	0.31	0.28	0.40
	^{3}He$+$Au	0.28	0.32	0.35	0.34	0.46

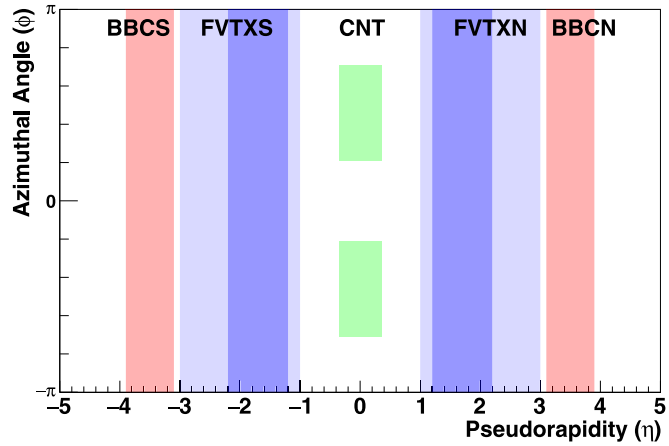

FIG. 1. PHENIX detector system layout. The Beam-Beam Counters (BBCS and BBCN), the Forward Vertex Tracker (FVTXS and FVTXN), and the central spectrometer arms (CNT) are shown with their respective pseudorapidity coverage (horizontal) and azimuthal coverage (vertical). For the FVTX, the lighter shaded region corresponds to the cluster acceptance while the darker shaded region corresponds to the reconstructed track acceptance.

frameworks are given in Table I. Additional negative binomial distribution fluctuations in particle production and subnucleonic structure tend to increase the eccentricities overall and reduce the differences, i.e., reducing the relative contribution from intrinsic geometry; however, significant intrinsic contributions remain in almost all cases. Additional measurements and theoretical work are needed to gain insight into the relative contributions to the initial geometry and thus further constrain both the hydrodynamic and prehydrodynamization stages.

Given the importance of these results, the PHENIX Collaboration has carried out a new analysis of the same data sets using combinations of three sets of detector combinations to extract two-particle correlations (2PC), called the 3×2PC method, to check the published results [16] and to provide additional information via correlations between particles from different kinematic regions. Because this makes use of three different two-particle correlations, it is called the 3×2PC method. In addition, because the PHENIX experiment collected its final data in 2016, we provide an archival set of correlation function data for future examination. In this paper, we do not compare the experimental results with the latest theoretical calculations and rather focus solely on the measurements and their quantified uncertainties.

II. ANALYSIS METHOD

The following subsections detail the PHENIX detector and the correlation analysis.

A. Detector description

The PHENIX detector is composed of multiple spectrometers and detector subsystems [26,27]. The detectors used in this analysis are highlighted in Fig. 1 and detailed here. The central arm spectrometers (CNT) measure charged hadrons with pseudorapidity $|\eta| < 0.35$. There are two CNT spectrometers, referred to as "east" and "west," each subtending $\Delta\phi = \pi/2$. The beam-beam counters (BBCs) [28] comprise two sets of 64 quartz Čerenkov radiators with photomultiplier readout, each set covering $3.1 < |\eta| < 3.9$: the BBC covering $-3.9 < \eta < -3.1$ is referred to as the "south" side (BBCS) and similarly the BBC covering $3.1 < \eta < 3.9$ is called the "north" side (BBCN). No individual particle information is available and the light output for each counter is normalized to the expected single charged particle response. We note that approximately half of the particles hitting the BBC are scattered from the beam pipe and the poles of the axial field magnet. The forward silicon vertex detector (FVTX) [29] comprises silicon strips oriented in the azimuthal direction and covers both forward and backward rapidity $1.0 < |\eta| < 3.0$. The FVTX can be used to count hits via clusters or via reconstructed tracks in the four layers on each side. The acceptance for FVTX tracks is significantly more constrained than the acceptance for clusters, and has a strong dependence on the z vertex of the collision (the direction along the beam line). Due to the orientation of the strips, there is no momentum information available with the FVTX tracks. The FVTX acceptance for tracks is shown in Fig. 2 and is dominated by tracks with $1.2 < |\eta| < 2.2$ and $p_T > 0.5$ GeV/c.

The BBC is used for triggering on minimum bias (MB) $p+$Au, $d+$Au, and ^{3}He$+$Au collisions by requiring a fast reconstructed z vertex within $|z| < 10$ cm and at least one hit on each side of the collision point. Additionally, a high-multiplicity trigger was employed to enhance the 0%–5% highest BBC multiplicity events by more than an order of magnitude. The BBC information in the Au-going direction is also used offline to select events in the 0%–5% centrality category. Full details are available in Refs. [10,11,14,16].

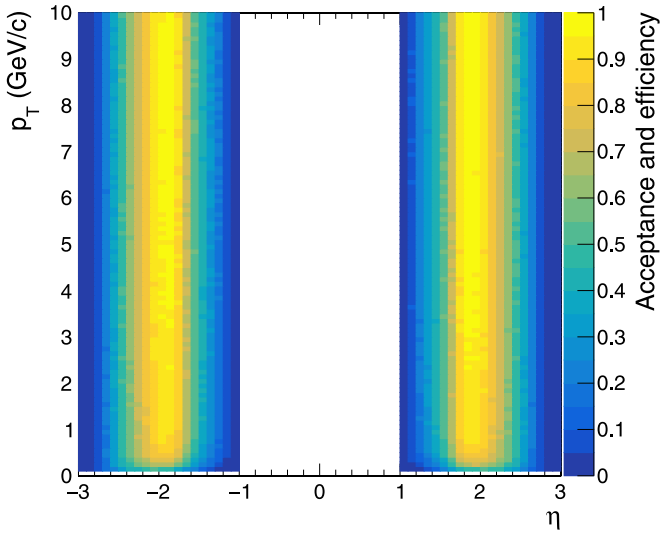

FIG. 2. PHENIX relative acceptance and efficiency for reconstructed tracks in the FVTX as a function of pseudorapidity and transverse momentum (p_T). The pseudorapidity and p_T acceptances depend on the collision z vertex, and the z-vertex distribution is included in generating this map. The tracking quality selection significantly reduces the efficiency for tracks with $p_T < 0.5$ GeV/c, again pseudorapidity dependent.

B. Event plane method

Previous PHENIX publications, including Ref. [16], utilized the event plane method [30] for measuring azimuthal anisotropies. The second- and third-harmonic event planes are determined in the BBC in the Au-going direction (referred to as the BBC "south" or BBCS) and in the Au-going FVTX (referred to as the FVTX "south" or FVTXS). The standard Q-vector recentering and event plane flattening techniques [31] are applied. Because the collision system is asymmetric, one cannot determine the event plane resolutions by comparing forward and backward detectors alone. Thus, the event plane resolutions are determined utilizing the three-detector combination BBCS-FVTXS-CNT.

It was recently pointed out that the third-harmonic event plane resolutions for the BBCS and FVTXS published in Ref. [16] do not follow the expected simple scaling of $R(\psi_n) \propto v_n\sqrt{N_{\rm hit}}$, where $N_{\rm hit}$ is the number of particles striking the event plane detector and v_n is the azimuthal anisotropy of those particles. We have carefully investigated this observation by running a full simulation of the event plane procedure, including the fact that the beam has nonzero angle and offset with respect to the detector coordinate system. The beam angles and offsets for the different running periods are given in Table II. An additional issue is that the PHENIX central carriage, which was moved between operation periods, has modest position offsets of order 1–2 mm relative to nominal. We find that the event plane flattening procedure in the rotated frame creates a distortion on the triangular anisotropy due to the elliptic anisotropy. The simulation qualitatively reproduced the event plane "bias" seen in real data; the effect largely cancels in the final v_3, because the bias is opposite between the BBCS and FVTXS. The effect is dependent on the size of the real signal v_3, the beam angle, beam offset, event multiplicity, and Q-vector recentering applied, and is much larger in $p+$Au and $d+$Au, where the smaller v_3 induces higher sensitivity to these effects.

TABLE II. System beam angles and offsets.

Year	System	$x_{\rm offset}$ (mm)	$y_{\rm offset}$ (mm)	x-z angle (mrad)
2014	^{3}He + Au	3.9	0.02	1.8
2015	p + Au	2.1	0.5	3.6
2016	d + Au	3.0	0.2	1.0

Because the experimental results for v_3 in $p+$Au and $d+$Au, where the distortion is largest, are important, we have carried out an independent analysis to examine the validity of the previous results. In the Monte Carlo simulation, two-particle correlation functions were successfully obtained when using an event-mixing acceptance correction in very fine bins in collision z vertex. Thus, we have carried out a new analysis of all three collision systems using three sets of two-particle correlations (3×2PC). In the limit of low event plane resolution, which is the case for all three systems, the event plane physics result and the 3×2PC physics result should agree [30]; this is because they are both estimators of $\langle v_2\rangle^{1/2}$ in this case, which means the sensitivity to both fluctuations and nonflow is the same.

We highlight that the analysis is independent of the published event plane results in the following ways: (1) a completely different code base is used; (2) the FVTX clusters are used in the event plane result but only FVTX tracks with good quality are used in the 3×2PC analysis; (3) additional systematic uncertainty checks are carried out as detailed below. Note that a subset of these 3×2PC checks were carried out in the $d+$Au published analyses detailed in Refs. [8,16]. In this paper, we also extend the kinematics from the original analysis to utilize different combinations of detectors in the 3×2PC method.

C. 3×2PC method

Here we detail the methodology used for the 3×2PC method. The 2PC technique utilized here follows the standard methodology [30]; the difference only coming in requiring three such 2PC because the collision systems are asymmetric. We measure the $\Delta\phi$ distribution of three different sets of pairs. In each pair, one particle is required to be in one subevent, and the other is required to be in another subevent. The manner in which the three different pairs of subevents are used is qualitatively very similar to the three-subevent method for determining the event plane resolution. In the limit of small event plane resolution, the techniques should yield the same results as they are sensitive to flow, flow fluctuations, and nonflow in the same manner [30].

The correlation function $C(\Delta\phi)$ is defined by

$$C(\Delta\phi) = \frac{S(\Delta\phi)}{M(\Delta\phi)}\frac{\int_0^{2\pi} M(\Delta\phi)}{\int_0^{2\pi} S(\Delta\phi)}, \quad (1)$$

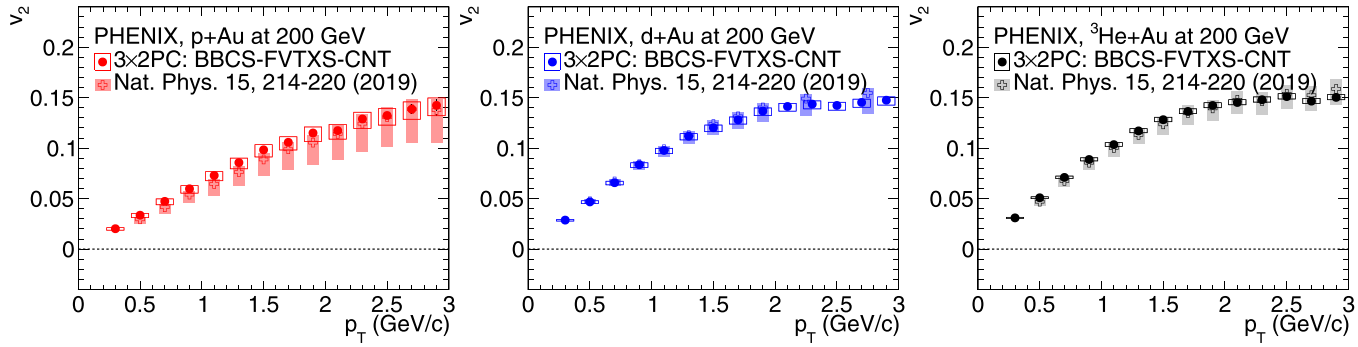

FIG. 3. The extracted v_2 coefficients as a function of p_T in 0%–5% central $p+$Au, $d+$Au, and ^{3}He +Au collisions from the 3×2PC method using the BBCS-FVTXS-CNT detector combination are shown as solid circles. Also shown as open crosses are the results published in Nature Physics [16] that were obtained via the event plane method and the same combination of detectors.

where $\Delta\phi$ is the difference in the azimuthal angles between the two particles in the pair; $S(\Delta\phi)$ is the signal distribution, which is constructed from pairs in which both particles are taken from the same event; and $M(\Delta\phi)$, which is the mixed event distribution, is constructed from pairs of particles in which each particle is required to be from a different event. It is essential that particles from mixed events come from the same *event category*, which includes centrality class and collision z-vertex class (i.e., the collision z vertices of both particles must be in the same collision z-vertex bin, typically 1 or 2 cm in width).

Once the correlation function is obtained, it can be decomposed via a Fourier series with coefficients c_n:

$$C(\Delta\phi) = 1 + \sum_{n=1} c_n \cos \Delta\phi, \tag{2}$$

where n is the harmonic number. Letting the superscripts denote subevents A, B, and C, the c_n coefficients mathematically represent

$$c_n^{AB} = \langle \cos[n(\phi_A - \phi_B)] \rangle = \langle v_n^A v_n^B \rangle, \tag{3}$$

$$c_n^{AC} = \langle \cos[n(\phi_A - \phi_C)] \rangle = \langle v_n^A v_n^C \rangle, \tag{4}$$

$$c_n^{BC} = \langle \cos[n(\phi_B - \phi_C)] \rangle = \langle v_n^B v_n^C \rangle. \tag{5}$$

Finally, the v_n in a single subevent can be determined as

$$v_n^C(p_T) = \sqrt{\frac{c_n^{AC}(p_T) c_n^{BC}(p_T)}{c_n^{AB}}}. \tag{6}$$

Note that it is also possible to determine the v_n in a different way, using only one correlation in the numerator and all three in the denominator:

$$v_n^C(p_T) = \frac{c_n^{AC}(p_T)}{\sqrt{c_n^{AB} c_n^{AC} / c_n^{BC}}}, \tag{7}$$

$$v_n^C(p_T) = \frac{c_n^{BC}(p_T)}{\sqrt{c_n^{AB} c_n^{BC} / c_n^{AC}}}; \tag{8}$$

where all of the correlations in the denominator are p_T integrated. For the detectors without momentum information (BBCS, FVTXS, FVTXN), this simply means all tracks or hits. For the detectors with momentum information (CNT), this means all tracks in the momentum range considered ($0.2 < p_T < 3.0$ GeV/c). Because this method is sometimes used by the LHC experiments, we will informally refer to it as the LHC-style v_n, in contrast to the PHENIX style discussed previously. Note that the PHENIX-style v_n is the geometric mean of the two possible LHC-style v_n. For that reason, the PHENIX style presents certain advantages, particularly for reduced systematic uncertainties.

D. Systematic uncertainties

The systematic uncertainties on the extracted v_2 and v_3 coefficients have multiple contributions. In previous analyses utilizing CNT tracks [10–12,14,16], contributions from variations in track quality criteria, run-to-run variations, etc. are quite modest and subdominant. The two dominant sources of systematic uncertainty result from comparing results with different collision z-vertex ranges and from comparing the two individual arms of the CNT. The uncertainty associated with the collision z vertex is assessed by comparing the nominal result with $|z| < 10$ cm to cases with $+4.0 < z < +10.0$ cm and $-10.0 < z < -4.0$ cm, because the changes in the FVTXS acceptance are significant over this range. We also consider the variation of only using "east" arm CNT tracks and only using "west" arm CNT tracks. The differences found in the systematic variations are taken to be the maximal possible deviations, representing asymmetric distributions about the central value. These differences are divided by $\sqrt{3}$ to give one standard deviation uncertainties, and then those individual uncertainties are added in quadrature.

For the results utilizing the FVTXS and FVTXN detectors, we have repeated the analyses using only one half, i.e., $1.2 < |\eta| < 1.7$, or the other half, i.e., $1.7 < |\eta| < 2.2$. These give similar results; however, we do not include the differences in the systematic uncertainties as the results may have differing contributions from nonflow and longitudinal decorrelations. These results are presented in the Appendix.

III. RESULTS

The main physics results from the 3×2PC analysis are the extracted $v_{2,3}$ coefficients as a function of charged hadron p_T at midrapidity $|\eta| < 0.35$. However, these values may depend

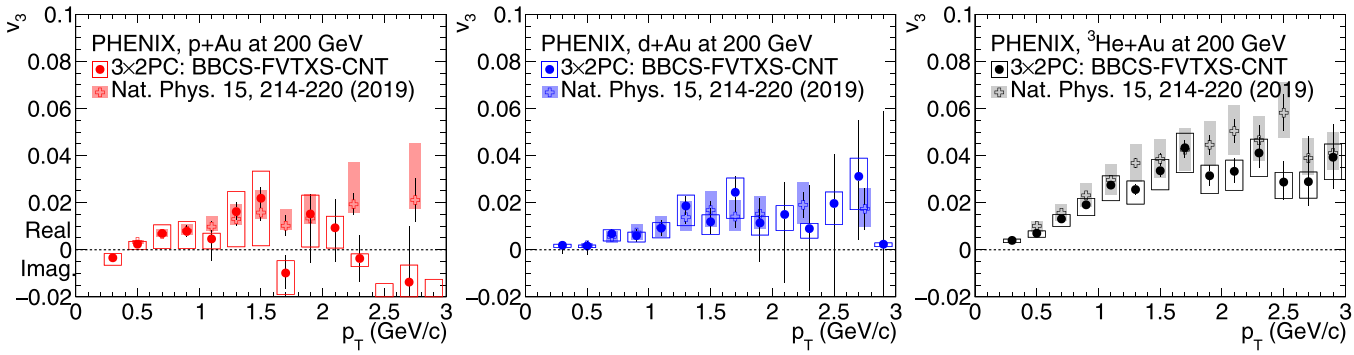

FIG. 4. The extracted v_3 coefficients as a function of p_T in 0%–5% central $p+$Au, $d+$Au, and ^{3}He$+$Au collisions from the 3×2PC method using the BBCS-FVTXS-CNT detector combination are shown as solid circles. Also shown as open crosses are the results published in Nature Physics [16] that were obtained via the event plane method and the same combination of detectors.

on the other two detectors used in combination with the CNT tracks. A set of example two-particle correlations and a complete set of extracted Fourier coefficients (c_1, c_2, c_3, c_4) and their statistical uncertainties are given in the Supplemental Material [32].

We highlight that care should be employed when comparing c_n coefficients directly as the p_T acceptance of the BBCS and FVTXS differ, as well as their relative particle (direct and scattered) contributions. Thus, even though in principle one can extract v_2 and v_3 values in the BBCS and FVTXS, by the same procedure as in the CNT, they do not have a straightforward physics interpretation. In the case of reconstructed, high quality FVTXS tracks, a full acceptance and efficiency correction as a function of collision z-vertex is possible, as done for example in Ref. [7]. However, a similar procedure has not been done for the BBCS, where approximately half the hits are from scattered particles.

A. v_n vs p_T results

Figure 3 shows the elliptic v_2 coefficients as a function of p_T from the 3×2PC method utilizing the three-detector combination BBCS-FVTXS-CNT. The results for the most central 0%–5% events are shown for all three collision geometries with statistical uncertainties as vertical lines and systematic uncertainties as open boxes. The systematic uncertainties have a high degree of point-to-point correlation. Also shown are the previously published v_2 coefficients [16] utilizing the event plane method. We highlight that the earlier publication includes an asymmetric systematic uncertainty estimate for nonflow based on a simple multiplicity scaling of coefficients from $p+p$ collisions at $\sqrt{s} = 200$ GeV; here we do not include this uncertainty, as we focus on what is directly measured from the correlation functions with all physics contributions included. The analysis presented here is in excellent agreement with the previously published results.

Figure 4 shows the third harmonic coefficient v_3 as a function of p_T. It is otherwise identical to the previous figure, showing a comparison between the present 3×2PC analysis and the previously published event plane analysis [16] for the most central 0%–5% events for all three collision systems and, as before, the vertical lines represent the statistical uncertainties and the boxes indicate the point-to-point correlated systematic uncertainties. There is good agreement within uncertainties between the two analyses, with the ^{3}He$+$Au v_3 values from the 3×2PC method slightly lower than the event plane results, though well within systematic uncertainties, which are largely independent between the two methods.

We highlight that the correlation coefficients c_2 and c_3 from all collision geometries follow the approximate expected scaling based on each detector's multiplicity and v_n using inputs from Ref. [7]. Thus the puzzle involving the nonscaling of the event plane values mentioned above is resolved.

B. Additional kinematic ranges

The above results are presented as v_2 and v_3 at midrapidity $|\eta| < 0.35$, but they can depend on the other two detectors used in the analysis, namely the BBCS and FVTXS. Nonflow contributions, longitudinal decorrelations, and po-

TABLE III. Pseudorapidity acceptances of individual detectors.

Detector	$\eta_{\min}$	$\eta_{\max}$
BBCS (tubes)	−3.9	−3.1
FVTXS (clusters)	−3.0	−1.0
FVTXS (tracks)	−2.2	−1.2
CNT (tracks)	−0.35	0.35
FVTXN (clusters)	1.0	3.0
FVTXN (tracks)	1.2	2.2

TABLE IV. Pseudorapidity acceptances of two-detector combinations.

Detector combination	$\lvert\Delta\eta\rvert_{\min}$	$\lvert\langle\Delta\eta\rangle\rvert$
BBCS-FVTXS (tubes-clusters)	0.1	1.8
BBCS-FVTXS (tubes-tracks)	0.9	1.8
BBCS-CNT (tubes-tracks)	2.75	3.5
FVTXS-CNT (clusters-tracks)	0.65	2.0
FVTXS-CNT (tracks-tracks)	0.85	2.0
FVTXN-CNT (clusters-tracks)	0.65	2.0
FVTXN-CNT (tracks-tracks)	0.85	2.0
FVTXS-FVTXN (clusters-clusters)	2.0	3.4
FVTXS-FVTXN (tracks-tracks)	2.4	3.4

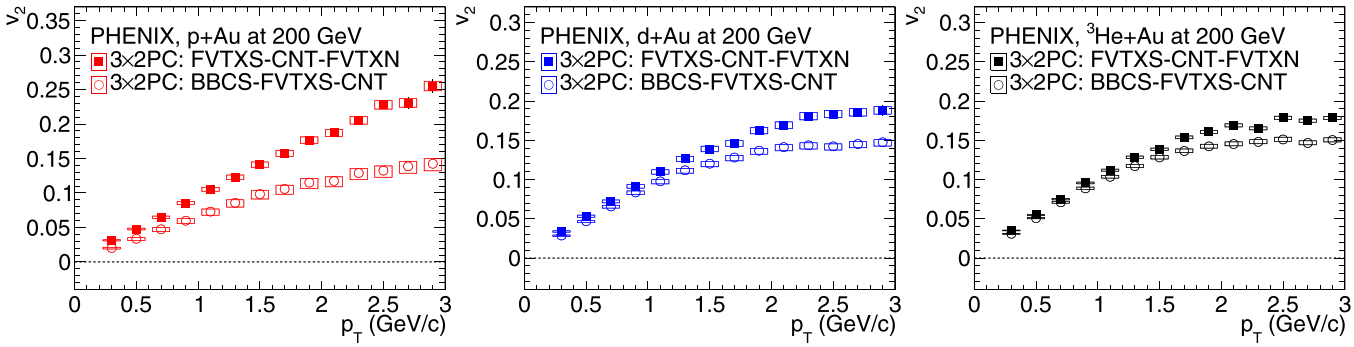

FIG. 5. The extracted v_2 coefficients as a function of p_T in 0%–5% central $p+$Au, $d+$Au, and ^{3}He +Au collisions from the 3×2PC method using the FVTXS-CNT-FVTXN detector combination are shown as solid squares. For comparison we also show the previously plotted results from the BBCS-FVTXS-CNT combination as open circles.

tentially other effects can make the extraction dependent on the kinematic coverage of the other detectors; see for example Ref. [33]. The original motivation for utilizing the BBCS and FVTXS is based on their higher multiplicity and significant pseudorapidity gap from the CNT tracks. Note that the gap should be thought of not in simple terms of the extreme $|\Delta\eta| > X$ value, but rather the distribution of possible $|\Delta\eta|$ values. Thus, the average $\langle|\Delta\eta|\rangle \approx 3.5, 2.0, 1.8$ for the BBCS-CNT, FVTXS-CNT, BBCS-FVTXS detector combinations.

We have also analyzed the detector combination FVTXS-CNT-FVTXN for the 3×2PC. Note that now the average values are $\langle|\Delta\eta|\rangle \approx 2.0, 2.0, 3.4$ for the FVTXS-CNT, CNT-FVTXN, and FVTXS-FVTXN detector combinations. However, based on measurements as a function of pseudorapidity in Ref. [7], the v_2 values are less than half the magnitude in the FVTXN compared to FVTXS and the multiplicity of tracks is also less than half. Thus, nonflow contributions relative to flow contributions are expected to be substantially larger in the FVTXN. Again, additional example correlation functions and the full set of extracted c_n coefficients are given in the Appendix.

Tables III and IV list the pseudorapidity acceptances of the different detectors and two-detector combinations. In Fig. 3 the pseudorapidity acceptance of the BBCS-FVTXS-CNT combination is listed as $-3.9 < \eta < -3.1, -3.0 < \eta < -1.0, |\eta| < 0.35$. In Fig. 5 the pseudorapidity acceptance of the FVTXS-CNT-FVTXN combination is listed as $-3.0 < \eta < -1.0, |\eta| < 0.35, 1.0 < \eta < 3.0$. While the full FVTX acceptance for clusters is $1.0 < |\eta| < 3.0$, this analysis predominantly uses tracks that are from $1.2 < |\eta| < 2.2$.

Figure 5 shows the elliptic v_2 coefficients as a function of p_T from the 3×2PC method utilizing the three-detector combination FVTXS-CNT-FVTXN. The results for the most central 0%–5% events are shown for all three collision geometries with statistical uncertainties as vertical lines and systematic uncertainties as open boxes. The systematic uncertainties have a high degree of point-to-point correlation. For comparison, the 3×2PC values from the BBCS-FVTXS-CNT combination are shown. Shown in Fig. 6 is the ratio of the v_2 in the FVTXS-CNT-FVTXN combination to the v_2 in the BBCS-FVTXS-CNT combination. We observe a modest 5%–15% difference in the ^{3}He +Au case, growing to a 10%–20% difference in the $d+$Au case, and then a rather large 35%–80% difference in the $p+$Au case. Qualitatively this difference could result from substantially larger nonflow contributions in the FVTXS-CNT-FVTXN combination, and this would be expected to be largest in the $p+$Au system which has the smallest multiplicity as well as the lowest expected elliptic flow itself. Nonflow effects are also expected to play a larger role at larger p_T, and we observe a modest rise in the ratios with p_T.

Figure 7 shows the third harmonic coefficient v_3 as a function of p_T from the 3×2PC using the FVTXS-CNT-FVTXN method, shown in solid squares, and also the BBCS-FVTXS-CNT detector combination, shown in open circles, for comparison. The statistical uncertainties are shown as vertical lines and the systematic uncertainties as open boxes. In the case of ^{3}He +Au, the results agree for the two detector combination sets within uncertainties. However, in the case of $p+$Au and $d+$Au, one of the c_3 coefficients is negative, and thus the mathematical calculation of v_3 results in

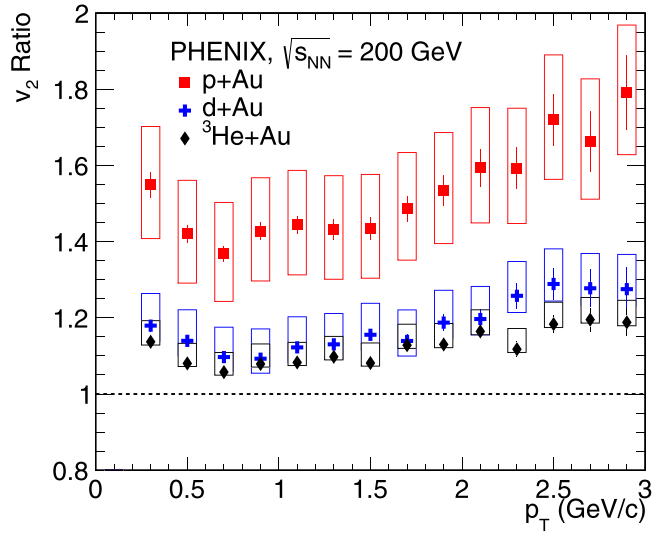

FIG. 6. Ratio of v_2 in the FVTXS-CNT-FVTXN combination (numerator) to v_2 in the BBCS-FVTXS-CNT combination (denominator) as a function of p_T for $p+$Au (red squares), $d+$Au (blue crosses), and ^{3}He +Au (black diamonds).

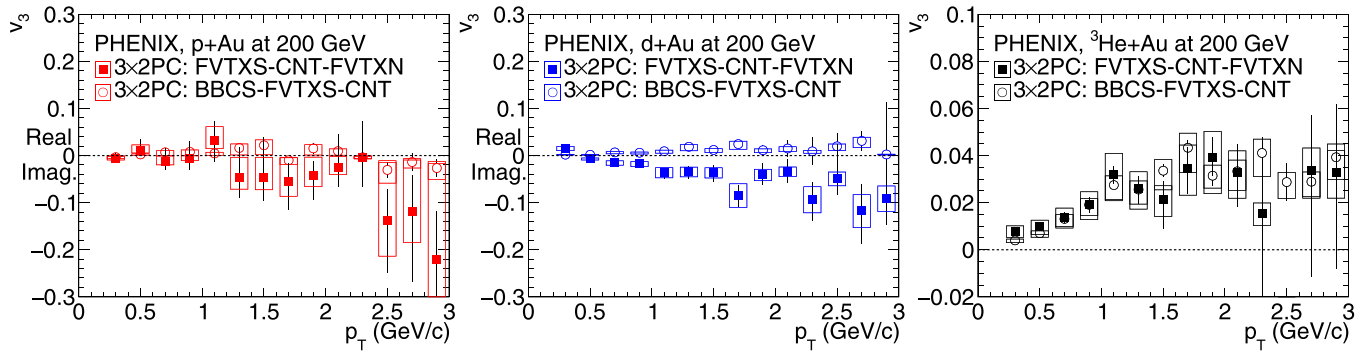

FIG. 7. The extracted v_3 coefficients as a function of p_T in 0%–5% central $p+$Au, $d+$Au, and ^{3}He$+$Au collisions from the 3×2PC method using the FVTXS-CNT-FVTXN detector combination are shown as solid squares. For comparison we also show the previously plotted results from the BBCS-FVTXS-CNT combination as open circles.

an imaginary value. These imaginary values are shown along the negative y axis in the figure.

These negative values of c_3 observed in the $p+$Au and $d+$Au systems are consistent with the observation that nonflow contributions in $p+p$ collisions extrapolated to these systems drive c_3 towards negative values. This effect is consistent with nonflow dominance in the FVTXS-CNT-FVTXN result. It is striking how much larger the effect is in $p+$Au and $d+$Au compared to negligible in ^{3}He$+$Au. Also, the difference in potential nonflow in the v_2 shown above is quite different between the systems and will also depend on the real triangular flow in these different geometries.

From the two-particle correlations and extracted coefficients (tabulated in the Supplemental Material [32]) one can examine the patterns between the two-particle kinematics and between collision systems. Access to the full suite of Fourier coefficients is critical to enable future analysis techniques to be applied and comparison with new theoretical tools that might more fully incorporate flow, nonflow, and longitudinal dynamics. Figure 8 shows the c_2 and c_3 coefficients from 0%–5% central $p+$Au, $d+$Au, ^{3}He$+$Au collisions from left to right. The markers are located at the pseudorapidity average from the two detectors [i.e., $(\eta_1+\eta_2)/2$] and the associated horizontal line extends between the two detectors (i.e., from

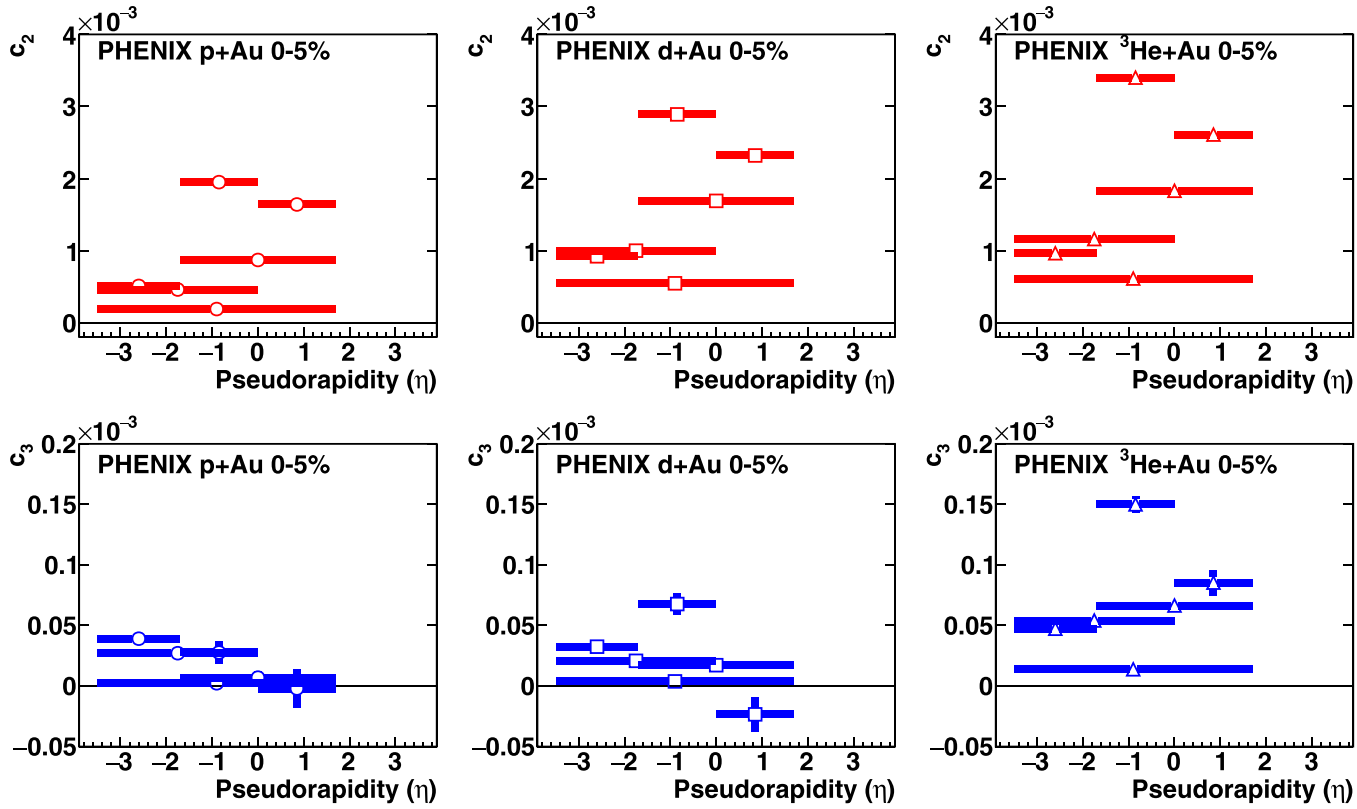

FIG. 8. Two-particle correlation c_2 and c_3 coefficients from 0%–5% central $p+$Au, $d+$Au, ^{3}He$+$Au collisions. The markers are located at the pseudorapidity average from the two detectors [i.e., $(\eta_1+\eta_2)/2$] and the associated horizontal line extends between the two detectors (i.e., from η_1 to η_2). The vertical bars indicate the statistical uncertainties. See text for details.

η_1 to η_2). Correlations involving tracks in the CNT (e.g., where one of the horizontal line end points is at $\eta = 0$) are for the inclusive range in $0.2 < p_T < 3.0\,\mathrm{GeV}/c$. As discussed in the Supplemental Material [32], the c_n coefficients should not be viewed as strict physics quantities because the charge in the BBC and tracks in the FVTX are not corrected for variations in acceptance, efficiency, and backgrounds, all of which can vary between running periods.

Starting with the c_2 values, one observes significant variation among the values from the different detector combinations used for the two-particle correlations. This arises naturally from the pseudorapidity dependence of the flow v_2 itself, and also from the different p_T coverage of the different detectors and different contributions from background, particularly in the BBCS. Overall one observes that the relative ordering of c_2 values from different combinations is qualitatively similar for the three collision systems, with the dominant feature that all of the $p+$Au values are lower.

For the c_3 values, the ordering of the detector combinations in ^{3}He +Au collisions is qualitatively similar to that of the c_2 values. In striking contrast, all of the c_3 coefficients (so all detector combinations) are significantly lower in $p+$Au and $d+$Au compared with ^{3}He +Au. This means that the conclusion of lower triangular flow in $p+$Au and $d+$Au is independent of any single detector used in the two-particle detector combination, i.e., it is seen in all combinations. In particular, c_3 values where the FVTXN is utilized, i.e., where the horizontal line extends to $\eta = +1.7$, are very low and in some cases actually negative, though with large statistical uncertainties. It is the negative value for c_3 between the CNT-FVTXN that results in the imaginary calculated v_3 in the FVTXS-CNT-FVTXN combination for $p+$Au and $d+$Au systems. Noting that the multiplicity is lowest in these systems at forward rapidity, i.e., the proton or deuteron-going direction, and the v_3 may be the smallest, the explanation may be from a large nonflow contribution toward negative values of c_3.

IV. SUMMARY

In this paper we have presented an independent analysis of the flow coefficients v_2 and v_3 as a function of p_T in 0%–5% central $p+$Au, $d+$Au, and ^{3}He +Au collisions at $\sqrt{s_{NN}} = 200$ GeV using the 3×2PC method. The results are in excellent agreement with the results published in Nature Physics from the PHENIX Collaboration using the event plane method [16]. In addition, variations in the kinematic selection for the three-detector combinations reveal an important role for nonflow and longitudinal decorrelations, particularly at forward rapidity, i.e., in the small projectile direction. To support future analyses, this paper includes an archival documentation of correlation functions from $p+p$ through ^{3}He +Au systems.

ACKNOWLEDGMENTS

We thank the staff of the Collider-Accelerator and Physics Departments at Brookhaven National Laboratory and the staff of the other PHENIX participating institutions for their vital contributions. We acknowledge support from the Office of Nuclear Physics in the Office of Science of the Department of Energy, the National Science Foundation, Abilene Christian University Research Council, Research Foundation of SUNY, and Dean of the College of Arts and Sciences, Vanderbilt University (U.S.A); Ministry of Education, Culture, Sports, Science, and Technology and the Japan Society for the Promotion of Science (Japan); Natural Science Foundation of China (People's Republic of China); Croatian Science Foundation and Ministry of Science and Education (Croatia); Ministry of Education, Youth and Sports (Czech Republic); Centre National de la Recherche Scientifique, Commissariat à l'Énergie Atomique, and Institut National de Physique Nucléaire et de Physique des Particules (France); J. Bolyai Research Scholarship, EFOP, the New National Excellence Program (ÚNKP), NKFIH, and OTKA (Hungary); Department of Atomic Energy and Department of Science and Technology (India); Israel Science Foundation (Israel); Basic Science Research and SRC(CENuM) Programs through NRF funded by the Ministry of Education and the Ministry of Science and ICT (Korea); Ministry of Education and Science, Russian Academy of Sciences, Federal Agency of Atomic Energy (Russia); VR and Wallenberg Foundation (Sweden); the U.S. Civilian Research and Development Foundation for the Independent States of the Former Soviet Union, the Hungarian American Enterprise Scholarship Fund, the US-Hungarian Fulbright Foundation, and the US-Israel Binational Science Foundation.

APPENDIX: v_n COEFFICIENTS WITH TWO DIFFERENT SUBSETS OF FVTX ACCEPTANCE

We have repeated the analyses of 3×2PC and dividing the FVTXS and FVTXN into halves, selecting tracks with either $1.2 < |\eta| < 1.7$ or $1.7 < |\eta| < 2.2$. Thus, the detector combinations will have increased or decreased rapidity gaps from the default analysis.

Figures 9 and 10 show the comparison of v_2 as a function of p_T at midrapidity using the two different FVTXN and FVTXS pseudorapidity ranges, in addition to the default use of the entire FVTX acceptance range. In all cases, the differences are modest. There is a general pattern that the v_2 calculated with the BBCS-FVTXS-CNT combination is slightly higher when using the FVTXS $1.2 < |\eta| < 1.7$ instead of FVTXS $1.7 < |\eta| < 2.2$. This may indicate a slight increase in nonflow contribution to the FVTXS-CNT correlation that dominates over a possible slight decrease in nonflow in the BBCS-FVTXS correlation. A similar effect is seen in the v_2 values with the FVTXS-CNT-FVTXN combination, which again may related to slightly larger nonflow contributions due to all correlations having a smaller rapidity gap.

Figures 11 and 12 show the comparison of v_3 as a function of p_T at midrapidity using the two different FVTXN and FVTXS pseudorapidity ranges, in addition to the default use of the entire FVTX acceptance range.

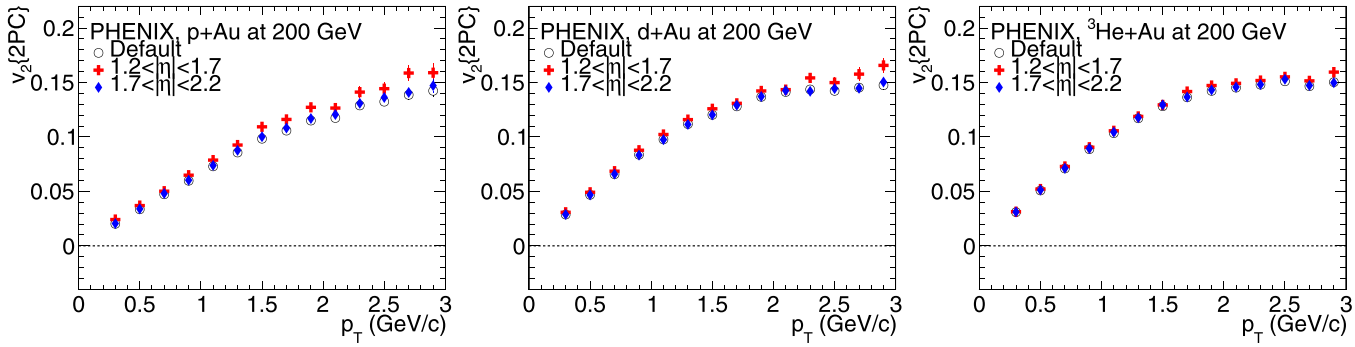

FIG. 9. Calculated midrapidity v_2 as a function of p_T for 0%–5% central $p+$Au, $d+$Au, ^{3}He +Au collisions. Shown are results from the BBCS-FVTXS-CNT combination including variations in the pseudorapidity selection of tracks in the FVTXS.

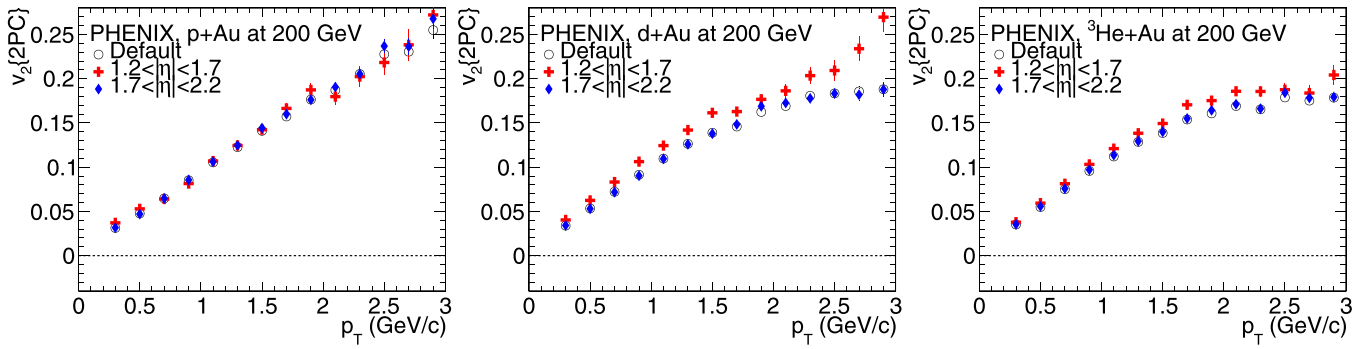

FIG. 10. Calculated midrapidity v_2 as a function of p_T for 0%–5% central $p+$Au, $d+$Au, ^{3}He +Au collisions. Shown are results from the FVTXS-CNT-FVTXN combination including variations in the pseudorapidity selection of tracks in the FVTXS and FVTXN.

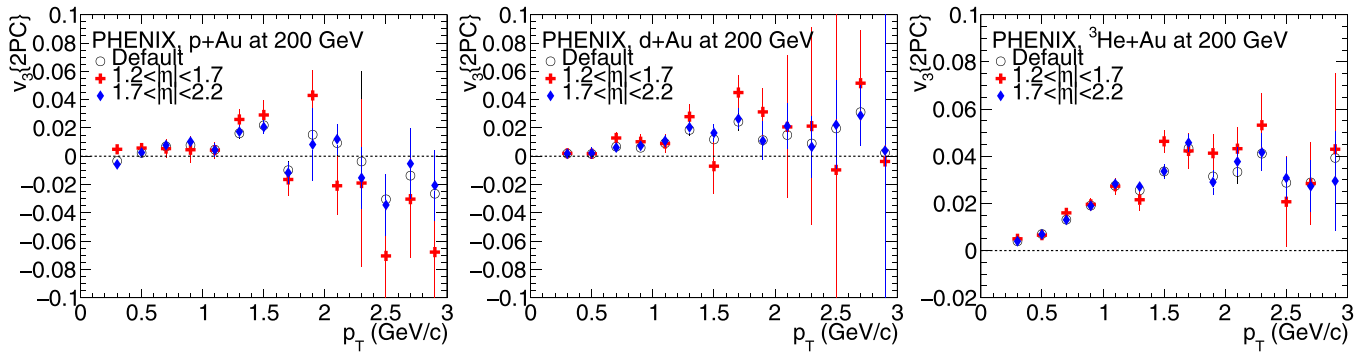

FIG. 11. Calculated midrapidity v_3 as a function of p_T for 0%–5% central $p+$Au, $d+$Au, ^{3}He +Au collisions. Shown are results from the BBCS-FVTXS-CNT combination including variations in the pseudorapidity selection of tracks in the FVTXS.

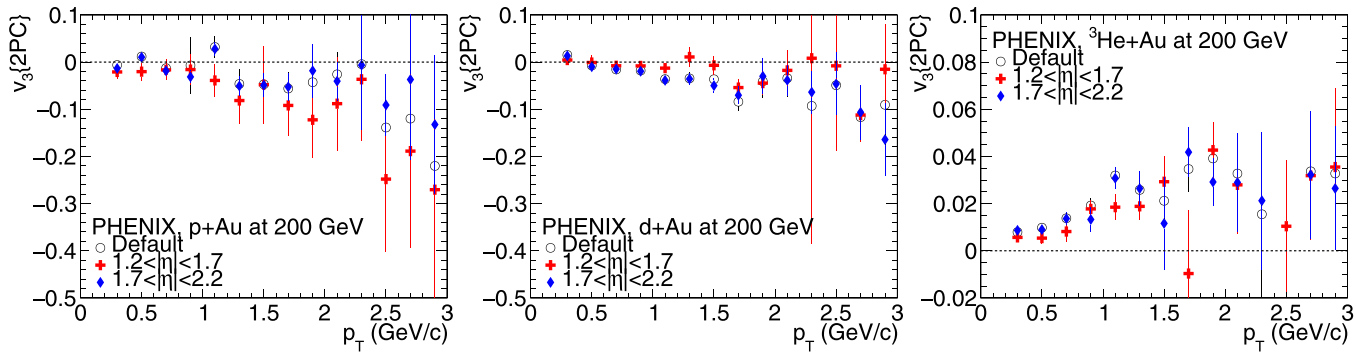

FIG. 12. Calculated midrapidity v_3 as a function of p_T for 0%–5% central $p+$Au, $d+$Au, ^{3}He +Au collisions. Shown are results from the FVTXS-CNT-FVTXN combination including variations in the pseudorapidity selection of tracks in the FVTXS and FVTXN.

In all cases, the differences are modest, though with larger statistical uncertainties when splitting the FVTX acceptance. The larger statistical uncertainties preclude any strong conclusions regarding a pattern with the different selections.

We do not include these differences as systematic uncertainties in the default v_2 and v_3 results as modest differences are expected. We can, however, rule out any large uncertainty from detector effects in the FVTX from the lower and higher rapidity acceptances.

[1] W. Busza, K. Rajagopal, and W. van der Schee, Heavy ion collisions: The big picture, and the big questions, Annu. Rev. Nucl. Part. Sci. **68**, 339 (2018).

[2] B. Müller, J. Schukraft, and B. Wyslouch, First results from Pb+Pb collisions at the LHC, Annu. Rev. Nucl. Part. Sci. **62**, 361 (2012).

[3] B. Müller and J. L. Nagle, Results from the relativistic heavy ion collider, Annu. Rev. Nucl. Part. Sci. **56**, 93 (2006).

[4] J. L. Nagle and W. A. Zajc, Small system collectivity in relativistic hadronic and nuclear collisions, Annu. Rev. Nucl. Part. Sci. **68**, 211 (2018).

[5] J. L. Nagle, A. Adare, S. Beckman, T. Koblesky, J. O. Koop, D. McGlinchey, P. Romatschke, J. Carlson, J. E. Lynn, and M. McCumber, Exploiting Intrinsic Triangular Geometry in Relativistic ^{3}He + Au Collisions to Disentangle Medium Properties, Phys. Rev. Lett. **113**, 112301 (2014).

[6] A. Adare *et al.* (PHENIX Collaboration), Spectra and ratios of identified particles in Au+Au and d+ Au collisions at $\sqrt{s_{NN}} =$ 200 GeV, Phys. Rev. C **88**, 024906 (2013).

[7] A. Adare *et al.* (PHENIX Collaboration), Pseudorapidity Dependence of Particle Production and Elliptic Flow in Asymmetric Nuclear Collisions of p + Al, p + Au, d + Au, and ^{3}He +Au at $\sqrt{s_{NN}} = 200$ GeV, Phys. Rev. Lett. **121**, 222301 (2018).

[8] C. Aidala *et al.* (PHENIX Collaboration), Measurements of azimuthal anisotropy and charged-particle multiplicity in d + Au collisions at $\sqrt{s_{NN}} = 200$, 62.4, 39, and 19.6 GeV, Phys. Rev. C **96**, 064905 (2017).

[9] C. Aidala *et al.* (PHENIX Collaboration), Measurements of Multiparticle Correlations in d + Au Collisions at 200, 62.4, 39, and 19.6 GeV and p + Au Collisions at 200 GeV and Implications for Collective Behavior, Phys. Rev. Lett. **120**, 062302 (2018).

[10] C. Aidala *et al.* (PHENIX Collaboration), Measurement of long-range angular correlations and azimuthal anisotropies in high-multiplicity p + Au collisions at $\sqrt{s_{NN}} = 200$ GeV, Phys. Rev. C **95**, 034910 (2017).

[11] A. Adare *et al.* (PHENIX Collaboration), Measurements of Elliptic and Triangular Flow in High-Multiplicity ^{3}He +Au Collisions at $\sqrt{s_{NN}} = 200$ GeV, Phys. Rev. Lett. **115**, 142301 (2015).

[12] A. Adare *et al.* (PHENIX Collaboration), Measurement of Long-Range Angular Correlation and Quadrupole Anisotropy of Pions and (Anti)Protons in Central d + Au Collisions at $\sqrt{s_{NN}} = 200$ GeV, Phys. Rev. Lett. **114**, 192301 (2015).

[13] A. Adare *et al.* (PHENIX Collaboration), Quadrupole Anisotropy in Dihadron Azimuthal Correlations in Central d + Au Collisions at $\sqrt{s_{NN}} = 200$ GeV, Phys. Rev. Lett. **111**, 212301 (2013).

[14] A. Adare *et al.* (PHENIX Collaboration), Measurement of emission angle anisotropy via long-range angular correlations with high p_T hadrons in d + Au and p + p collisions at $\sqrt{s_{NN}} =$ 200 GeV, Phys. Rev. C **98**, 014912 (2018).

[15] A. Adare *et al.* (PHENIX Collaboration), Measurements of mass-dependent azimuthal anisotropy in central p + Au, d + Au, and ^{3}He +Au collisions at $\sqrt{s_{NN}} = 200$ GeV, Phys. Rev. C **97**, 064904 (2018).

[16] C. Aidala *et al.* (PHENIX Collaboration), Creation of quark-gluon plasma droplets with three distinct geometries, Nat. Phys. **15**, 214 (2019).

[17] C. Shen, J.-F. Paquet, G. S. Denicol, S. Jeon, and C. Gale, Collectivity and electromagnetic radiation in small systems, Phys. Rev. C **95**, 014906 (2017).

[18] M. Mace, V. V. Skokov, P. Tribedy, and R. Venugopalan, Hierarchy of Azimuthal Anisotropy Harmonics in Collisions of Small Systems from the Color Glass Condensate, Phys. Rev. Lett. **121**, 052301 (2018); **123**, 039901(E) (2019).

[19] M. Mace, V. V. Skokov, P. Tribedy, and R. Venugopalan, Systematics of azimuthal anisotropy harmonics in proton-nucleus collisions at the LHC from the color glass condensate, Phys. Lett. B **788**, 161 (2019); **799**, 135006(E) (2019).

[20] J. L. Nagle and W. A. Zajc, Assessing saturation physics explanations of collectivity in small collision systems with the IP-Jazma model, Phys. Rev. C **99**, 054908 (2019).

[21] B. Schenke, C. Shen, and P. Tribedy, Hybrid Color Glass Condensate and hydrodynamic description of the Relativistic Heavy Ion Collider small system scan, Phys. Lett. B **803**, 135322 (2020).

[22] P. Romatschke, Light-heavy ion collisions: A window into pre-equilibrium QCD dynamics? Eur. Phys. J. C **75**, 305 (2015).

[23] J. D. Orjuela Koop, A. Adare, D. McGlinchey, and J. L. Nagle, Azimuthal anisotropy relative to the participant plane from a multiphase transport model in central p+ Au, d+ Au, and ^{3}He +Au collisions at $\sqrt{s_{NN}} = 200$ GeV, Phys. Rev. C **92**, 054903 (2015).

[24] K. Welsh, J. Singer, and U. W. Heinz, Initial state fluctuations in collisions between light and heavy ions, Phys. Rev. C **94**, 024919 (2016).

[25] B. Schenke, P. Tribedy, and R. Venugopalan, Fluctuating Glasma Initial Conditions and Flow in Heavy Ion Collisions, Phys. Rev. Lett. **108**, 252301 (2012).

[26] K. Adcox *et al.* (PHENIX Collaboration), PHENIX detector overview, Nucl. Instrum. Methods Phys. Res., Sect. A **499**, 469 (2003).

[27] H. Akikawa *et al.* (PHENIX Collaboration), PHENIX muon arms, Nucl. Instrum. Methods Phys. Res., Sect. A **499**, 537 (2003).

[28] M. Allen *et al.*, PHENIX inner detectors, Nucl. Instrum. Methods Phys. Res., Sect. A **499**, 549 (2003), special issue: The Relativistic Heavy Ion Collider Project: RHIC and its Detectors.

[29] C. Aidala *et al.*, The PHENIX Forward Silicon Vertex Detector, Nucl. Instrum. Methods Phys. Res., Sect. A **755**, 44 (2014).

[30] J.-Y. Ollitrault, A. M. Poskanzer, and S. A. Voloshin, Effect of flow fluctuations and nonflow on elliptic flow methods, Phys. Rev. C **80**, 014904 (2009).

[31] A. M. Poskanzer and S. A. Voloshin, Methods for analyzing anisotropic flow in relativistic nuclear collisions, Phys. Rev. C **58**, 1671 (1998).

[32] See Supplemental Material at http://link.aps.org/supplemental/10.1103/PhysRevC.105.024901 for a set of example two-particle correlations and a complete set of extracted Fourier coefficients (c_1, c_2, c_3, c_4) and their statistical uncertainties

[33] S. H. Lim, Q. Hu, R. Belmont, K. K. Hill, J. L. Nagle, and D. V. Perepelitsa, Examination of flow and nonflow factorization methods in small collision systems, Phys. Rev. C **100**, 024908 (2019).